

pubs.acs.org/journal/ascecg Research Article

Synthesis and Optical Properties Based on Ni-Doped Zn₂SiO₄ Blue Pigments with High-NIR Reflectance

Qiuying Wang, Zhiwei Wang, Menghang Qi, Hang Zhao, Xin Xin, Anjali Verma, Theeranun Siritanon, Arthur P. Ramirez, M.A. Subramanian, and Peng Jiang*



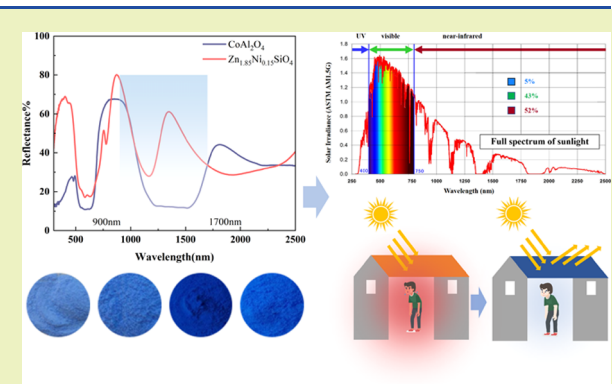
Cite This: ACS Sustainable Chem. Eng. 2024, 12, 5522-5532



ACCESS

Metrics & More

ABSTRACT: The severe urban heat island effect emphasizes the heightened importance of reducing building energy consumption. Cool pigments with higher near-infrared reflectivity contribute to the overall coating performance of the building. In this work, a novel intense blue pigment with superior infrared reflectance based on Ni-doped $\rm Zn_2SiO_4$ was successfully synthesized via the simple solid-state method. The crystal structure, oxidation states, and optical properties are analyzed. The oxidation state of Ni was confirmed to be +2 using magnetic analysis and XPS. The intense blue color exhibited by the solid solution is due to the ${}^3\rm T_1({}^3\rm F) \rightarrow {}^3\rm T_1({}^3\rm P)$ transition of Ni²⁺ at the tetrahedral sites. UV–vis–NIR spectra demonstrate that this pigment exhibits superior near-infrared reflectance compared to cobalt blue in the range of 900–1700 nm, indicating its potential application in the realm of building energy conservation.



Article Recommendations

KEYWORDS: Zn₂SiO₄, cool blue pigments, high-NIR reflectance, optical properties, solid-state method

1. INTRODUCTION

The process of urbanization has given rise to a range of environmental issues, one of which is the heat island effect. Changes in urban climate not only lead to energy wastage and increased carbon emissions but also have adverse effects on people's health and quality of life. With the ongoing global warming, cities are facing more severe challenges. 1-6 According to statistics, in some developed countries, building energy consumption accounts for 40% of the total energy consumption, and its related greenhouse gas emissions also account for 40% of the total emissions. Near-infrared region (NIR, 700–2500 nm) constitutes the majority, approximately 52% (Figure 1), of the solar spectrum. Therefore, when high near-infrared reflectance coatings are applied to building surfaces, they can effectively reduce surface temperatures, thereby alleviating the effect of the urban heat island effect.

In colored high-near-infrared (NIR) reflective coatings, the cool pigment with superior NIR reflectivity contributes to the overall performance. Currently, the industrialized blue pigments ready for coatings are majorly based on ultramarine (Na₆Al₄Si₆S₄O₂₀) and cobalt blue (CoAl₂O₄). However, their NIR reflectance is limited and, therefore, lowers the cooling effect of the coating. Moreover, ultramarine easily decomposes under acidic conditions to produce toxic hydrogen sulfide gas, Cobalt blue contains the toxic ion Co²⁺ and is expensive. In 2009, Subramanian developed a new type

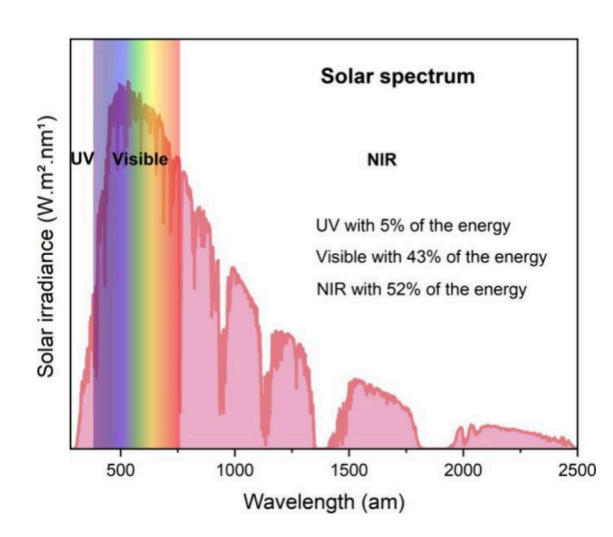


Figure 1. Wavelength light versus spectral irradiance over the Air Mass AM1.5 solar spectrum.⁹

Received: December 5, 2023 Revised: March 12, 2024 Accepted: March 12, 2024 Published: March 26, 2024





of intense blue pigment based on the YIn_{1-x}Mn_xO₃ solid solution with satisfied NIR reflectance, and it is ideal for the cool blue pigment. Research studies have been conducted, and even higher NIR reflectance could be achieved by Li doping or combining with ZnO. However, the high price of the precursor In₂O₃ is the main obstacle for its large-scale applications.^{6,15} Therefore, the exploration of suitable new high near-infrared reflective blue pigments holds considerable research significance. Currently, the primary chromophoric ion responsible for blue coloration is Co²⁺. However, Co²⁺ is expensive and environmentally polluting. ^{16–18} Previous research results show that when Ni²⁺, Cu²⁺, and Mn⁵⁺ are in the tetrahedral coordination environment, a blue hue is possibly produced. 19-21 However, it is important to note that Mn5+ ions are inherently unstable and prone to disproportionate to Mn⁷⁺ and Mn4+.22 In the case of Ni2+, previous research has effectively produced various blue hues by Ni^{2+} doping in regular tetrahedral coordination in structures such as CaAl₁₂O₁₉, ²³ BaAl₁₂O₁₉, ²⁴ MgAl₂O₄, ²⁵ and so on. When Ni²⁺ resides in distorted tetrahedral positions, it exhibits different colors such as magenta and lilac, ^{26,27} as shown in Figure 2.

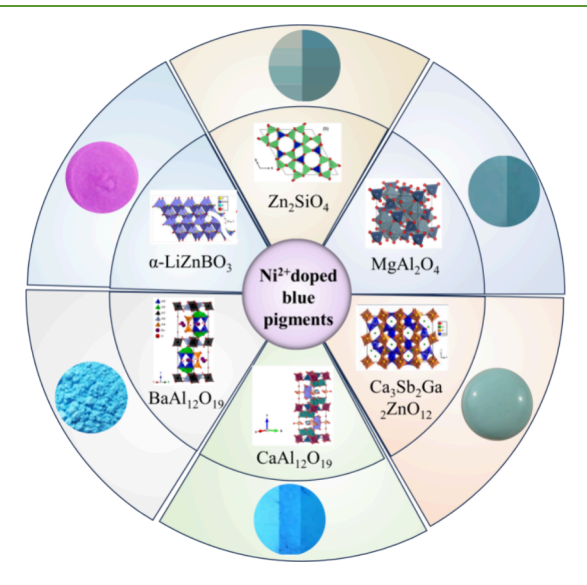


Figure 2. Doping of Ni^{2+} at tetrahedral positions in different oxides. $^{19,20,23-26,30,31}$

However, these pigments have the problems of complicated preparation, expensive price, or poor color performance, and an intense blue hue has not yet been achieved by Ni²⁺ into tetrahedral coordination. Therefore, one direction in the synthesis of novel blue pigments involves the quest for materials possessing a stable tetrahedral coordination structure capable of accommodating Ni²⁺. ^{28,29}

Widely used in phosphors, adsorbents, electronic insulators, batteries, and glaze, $\rm Zn_2SiO_4$, which is an important inorganic functional material with high-temperature stability, crystallizes in a willemite structure (shown in Figure 3). $^{32-35}$ Zinc (Zn) and silicon (Si) atoms occupy two tetrahedral positions within the lattice, displaying a rhombic symmetry. 31,36 This structural feature exclusively entails tetrahedral coordination, thereby establishing a stable environment conducive to Ni²⁺ incorporation

Research endeavors centered on $\rm Zn_2SiO_4$ primarily involve its crystallographic attributes, synthetic methodologies, and applications in fluorescence. The most studied is its

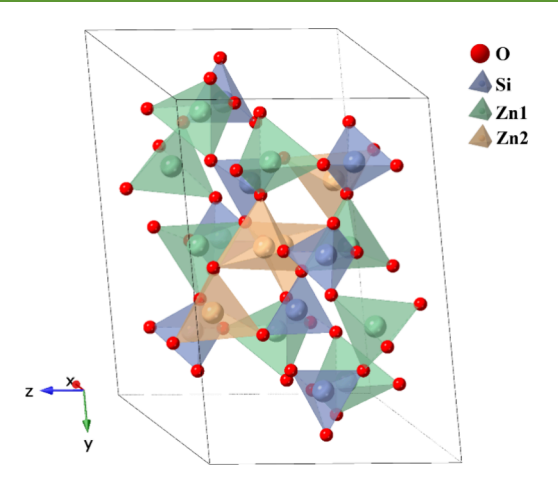


Figure 3. Crystal structure of Zn_2SiO_4 (purple tetrahedra are Si atoms, green are Zn1 atoms, orange are Zn2 atoms).

fluorescence performance. Mn-doped $\rm Zn_2SiO_4$ green phosphors were synthesized by different methods by Singh et al., ³⁸ Diao and Yang, ⁴⁰ and Portakal-Uçar et al. ⁴¹ Previous research on pigments has covered the doping of Mn²⁺, Co²⁺, and Ni²⁺ ions into the structure. ^{30,31,42–45} These doping efforts, conducted through calcination at temperatures ranging from 900 to 1300 °C, have yielded blue, bright yellow, blue-green, and green pigments. Among these pigments, the most intense blue hues were achieved through Co²⁺ doping. These studies have comparatively limited investigations into the performance of pigments derived from Ni²⁺ doping.

Therefore, in this study, Ni-ion-doped $\rm Zn_2SiO_4$ was synthesized by the conventional solid-phase method. Nickel ions replace zinc ions at their tetrahedral sites, yielding a deep intense blue pigment with greater color intensity than cobalt blue through a small amount of Ni doping. The pigments are stable and pure phase, and the doping of Ni has been greatly reduced compared to previous studies. Optical tests indicated a high near-infrared reflectance, suggesting potential applications in cool pigment applications.

2. EXPERIMENTAL SECTION

2.1. Sample Preparation. $Zn_{2-x}Ni_xSiO_4$ (0.05 $\leq x \leq$ 0.2) was synthesized by a conventional high-temperature solid-phase method. Stoichiometric ZnO oxide (99.96% purity, Bide Pharmaceuticals, China), NiO oxide (99.0% purity, Aladdin, China), and silica SiO₂ (99.0% purity, Aladdin, China) were weighed and mixed in an onyx ball milling jar under an alcohol medium for grinding and mixing. Subsequently, the mixed samples were dried and sintered in an oxygen atmosphere. The sintering condition was 1400 °C for 2 h. Finally, the sintered samples were ground to obtain the pigments, which were used for subsequent characterization.

The synthesized pigments were dispersed into acetic acid and ammonia solutions for the acid—base resistance test, adjusting the pH to 3 and 12, respectively, and immersed at room temperature for 6 h. The solution was then washed with deionized water to a pH of 7. Finally, the pigment powders were dried in an oven at 60 $^{\circ}$ C to remove residual moisture.

2.2. Characterization. X-ray diffraction (XRD) patterns of all of the synthesized powder samples were collected on a Rigaku miniflex 600 X-ray diffractometer. The data were acquired using Cu K α (λ = 0.15415 nm) radiation in the 2θ range of $10^{\circ}-90^{\circ}$ at a speed of $5^{\circ}/$ min. XRD data were refined by the Rietveld method using Fullprof software.

The oxidation state of Ni was determined by X-ray photoelectron spectroscopy (XPS) and magnetic testing. The XPS equipment used was a Thermo Scientific K-Alpha X-ray photoelectron spectrometer.

Monochromatic AlKa (Mono AlKa) sources were used for data acquisition at an energy of 1486.6 eV. Magnetic data were collected on the Quantum Design Physical Properties Measurement System (PPMS) in the temperature range of 0–350 K. The experimental effective magnetic moments between 150 and 300 K were then calculated by the equation:

$$\mu_{\text{eff}}(\exp) = \sqrt{\frac{3KC}{N_{\text{A}}}} = 2.84\sqrt{C}\mu_{\text{B}}$$
(1)

where k is Boltzmann's constant, C is Curie constant, $N_{\rm A}$ is Avogadro's number, and $\mu_{\rm B}$ is the Bohr magneton. The theoretical effective magnetic moment was calculated by the equation:

$$\mu_{\text{eff}}(\text{th}) = \sqrt{4S(S+1)}\,\mu_{\text{B}} \tag{2}$$

where *S* is the total spin quantum number.

A 3nh YS3060 spectrophotometer was used to test the L^* a^* b^* color parameters of the samples. L^* represents the brightness; its value from 0 to 100 indicates dark to bright. a^* represents the redgreen value, a^* is positive for red and conversely for green. b^* represents the yellow-blue value, and b^* is positive for yellow and conversely for blue.

UV—vis-NIR absorption patterns were obtained using a UV—vis-NIR spectrophotometer. The equipment used was an Agilent Cary 7000 UV—vis-NIR spectrophotometer. The data was collected in an integrating sphere mode at a scanning speed of 600 nm/min. $\rm BaSO_4$ is used as a substrate for baseline correction.

The NIR solar reflectance (R^*) of pigments within the wavelength range spanning from 700 to 2500 nm was ascertained using the following equation:

$$R^* = \frac{\int_{700}^{2500} r(\lambda)i(\lambda)d\lambda}{\int_{700}^{2500} i(\lambda)d\lambda}$$
(3)

In the equation, $r(\lambda)$ represents the spectral reflectance derived from experimental data, while $i(\lambda)$ signifies the solar spectral irradiance obtained from the ASTM G173-03 Reference Spectra standard (W m⁻² nm⁻¹).¹

3. RESULTS AND DISCUSSION

3.1. XRD Analysis. The XRD patterns of the pigments of $Zn_{2-x}Ni_xSiO_4$ (0.05 $\leq x \leq$ 0.3) powder calcined at 1400 °C are shown in Figure 4. The main phase of all of the synthesized samples belongs to the Zn₂SiO₄ willemite phase (PDF#85-0453). The diffraction peaks correspond well with the standard data of Zn₂SiO₄, and the impurity phase is not detected. The sharp peak shape of the diffraction peak indicates the good crystallinity of the as-synthesized samples. The diffraction peaks between 2θ of $30-35^{\circ}$ are magnified, as shown in Figure 4b. As the ion radius of Ni²⁺ is slightly smaller than that of Zn²⁺, the crystal structure will not be significantly distorted. From the figure, it can be seen that the (11-3) crystal faces move at a small angle, which may be due to the formation of NiO clusters as the Ni²⁺-doping amount increases. ^{47,48} When the doping concentration of Ni²⁺ is 0.3, an impurity peak of NiO appears, indicating that the doping concentration limit of Ni^{2+} is 0.2.

In order to explore the performance differences between low and high temperatures, various calcination temperatures from 1100 to 1500 °C for $\rm Zn_{1.85}Ni_{0.15}SiO_4$ were studied, and the XRD results and apparent color are compared in Figure 5. The changes in XRD peaks and apparent colors of the pigments reveal distinct changes with/without impurity. It is observed from Figure 5 that at sintering temperatures of 1100 and 1200 °C, the samples exhibit a distinct green hue. At this point, the impurity peaks of ZnO and NiO are very high, indicating an

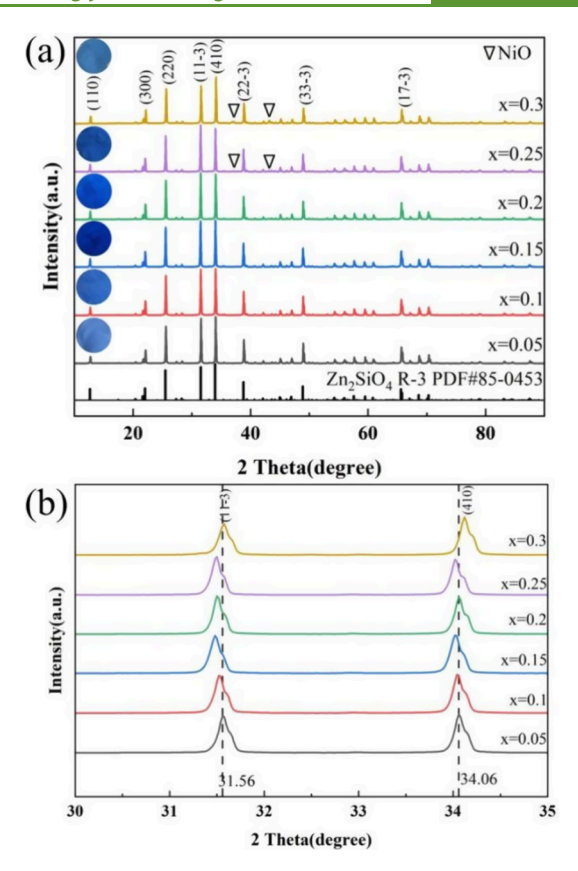


Figure 4. (a) XRD patterns of $Zn_{2-x}Ni_xSiO_4$ (0.05 $\leq x \leq$ 0.3) powders. (b) Enlarged XRD pattern (30–35°).

incomplete reaction. As the temperature rises to 1300 and 1350 °C, a noticeable shift toward a blue tint occurs, resulting in a blue-green color. The intensities of the NiO and ZnO peaks significantly diminish, indicating the partial integration of NiO into the crystal lattice. It is worth noting that, at 1400 °C, a remarkable change occurs, with the samples taking on a deep, vibrant blue color. With continued temperature elevation, the peaks of NiO and ZnO become lower, and the blue hue intensifies. With continued temperature elevation, the peaks of NiO and ZnO become lower and the blue hue intensifies. In addition, the diffraction peaks at 31.48° and 34.02° shift to the left, indicating a shrinkage of the lattice. This is because the ionic radius of Ni²⁺ (0.63 Å) is slightly smaller than that of Zn²⁺ (0.74 Å).⁴⁹ Meanwhile, NiO and ZnO impurity peaks disappear, yielding a phase-pure XRD pattern. This indicates complete NiO integration into the crystal structure at this point. From Table 1, the stoichiometric ratio of Ni^{2+} in $Zn_{1.85}Ni_{0.15}SiO_4$ is close to 0.15 by calculating the occupancy rate of Ni²⁺. It also proves that Ni atoms have completely entered Zn₂SiO₄. At temperatures exceeding 1400 °C, the samples melt after the sintering process, indicating the upper sintering temperature limit of 1400 °C for these pigments.

The XRD patterns of $Zn_{2-x}Ni_xSiO_4$ (0.05 $\leq x \leq 0.2$) are refined with the $R_{\overline{3}}$ space group by the Rietveld method using Fullprof software. The refined pattern and the lattice parameters of typical samples are shown in Figures 6 and 7, the refined crystallographic data are summarized in Table 1, and the refined atomic coordinates of $Zn_{1.85}Ni_{0.15}SiO_4$ are shown in Table 2. The refined R-factor values fall within an acceptable range, indicating the reliability of the refinement

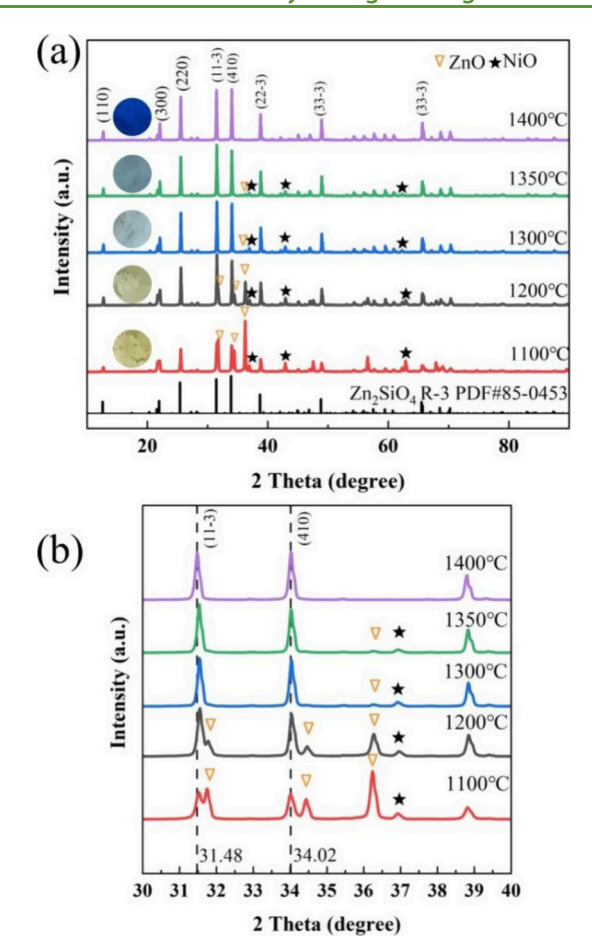


Figure 5. (a) XRD patterns of $Zn_{1.85}Ni_{0.15}SiO_4$ powders at different temperatures. (b) Enlarged XRD pattern (30–40°).

Table 1. Crystallographic Data, Occupancy Factor (Occ.), and Average Interatomic Distances for $Zn_{2-x}Ni_xSiO_4$ (0.05 $\leq x \leq 0.2$) Powder after Refined

General Information					
Space gro	oup		R-3		
Sample	Zn ₂ SiO ₄	Zn _{1.95} Ni _{0.05} SiO ₄	Zn _{1.9} Ni _{0.1} SiO ₄	Zn _{1.85} Ni _{0.15} SiO ₄	Zn _{1.8} Ni _{0.2} SiO ₄
a(Å)	13.948	13.932(20)	13.930(18)	13.926(3)	13.922(3)
c(Å)	9.3150	9.3138(15)	9.3201(13)	9.3265(20)	9.3288(20)
a/c	1.4970	1.4959	1.4946	1.4932	1.4924
$V({\rm \AA}^3)$	1569.4	1565.7(0.040)	1566.2(0.036)	1566.4(0.056)	1566.0(0.061)
Occ.					
Znl	1.0000	0.9680(0)	0.9500(2)	0.9210(2)	0.9030(3)
Ni1	-	0.0320(0)	0.0500(2)	0.0790(2)	0.0970(3)
Zn2	1.0000	0.9750(3)	0.9320(0)	0.9460(0)	0.8450(0)
Ni2	-	0.0250(3)	0.0680(0)	0.0540(0)	0.1550(0)
Average i	interatomic	distances (Å)	O2 Zal	03	
Zn1-O	1.9500	1.9490	1.9480	1.9328	1.9865
Zn2-O	1.9610	1.9773	1.9660	1.9753	1.9025

results. When Ni^{2+} and Zn^{2+} are in tetrahedral coordination, their ionic radii are 0.55 and 0.60 Å, ⁵⁰ respectively. Following Ni^{2+} doping, in comparison to the original crystal structure, a and b lattice parameters, as well as the unit cell volume, exhibit

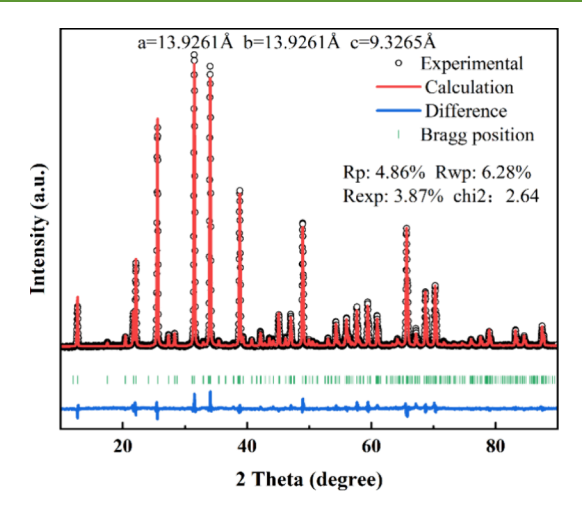
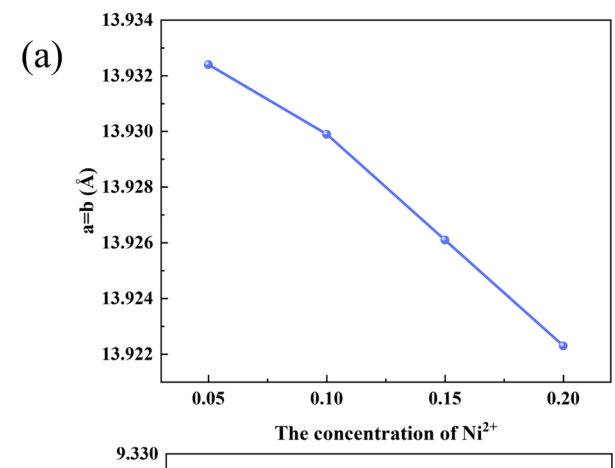


Figure 6. Rietveld refinement of XRD data for $Zn_{1.85}Ni_{0.15}SiO_4$ powder.



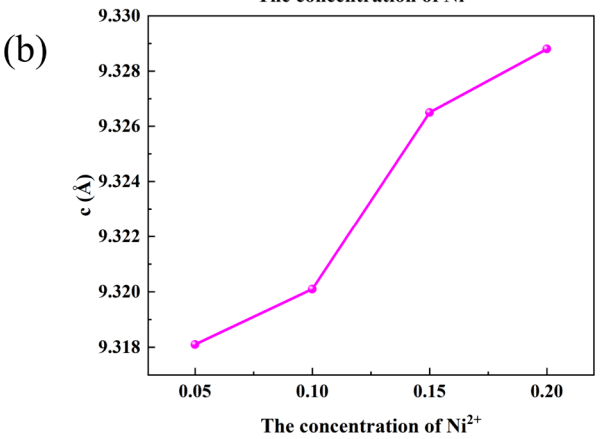


Figure 7. (a) A and b and (b) c lattice parameters vary for $Zn_{2-x}Ni_xSiO_4$ (0.05 $\leq x \leq 0.2$) synthesized powders.

a reduction, whereas the c lattice parameter increases, resulting in a gradual decrease in the a/c ratio. This pattern is also observed in $\text{Co}^{2+}\text{-doped}$ $\text{Zn}_2\text{SiO}_4.^{51}$ This phenomenon is possibly attributed to the influence of the $\text{Ni}^{2+}\text{-doping}$ concentration on the random distribution of Ni^{2+} ions or the localized defects it induces. This observation serves as evidence of the successful incorporation of Ni^{2+} into the Zn sites. 52

When the Ni²⁺-doping amount is 0.05 and 0.15, the occupancy (Occ.) value of Ni²⁺ at the Zn1 site exceeds that at the Zn2 site, and the situation is reversed when the doping

Table 2. Atomic Coordinates for Zn_{1.85}Ni_{0.15}SiO₄ Powders after Being Refined

site	\boldsymbol{x}	у	z
Zn1	0.9809(20)	0.1904(29)	0.4158(68)
Ni1	0.9809(20)	0.1904(29)	0.4158(68)
Zn2	0.9757(22)	0.1917(28)	0.0818(66)
Ni2	0.9757(22)	0.1917(28)	0.0818(66)
Si	0.9802(43)	0.1904(41)	0.7529(151)
O1	0.1147(72)	0.2122(89)	0.7479(202)
O2	-0.0080(106)	0.3114(76)	0.7340(123)
O3	0.9261(109)	0.1211(98)	0.8933(190)
O4	0.9246(105)	0.1243(112)	0.6018(185)

amount is 0.1 and 0.2, as shown in Table 1. This phenomenon was also observed when we assume that Ni²⁺ occupies only one of the Zn1 and Zn2 positions for refinement. This observation may be ascribed to the relatively similar crystal environments of the Zn1 and Zn2 sites, so Ni²⁺ is randomly distributed at the Zn1 site and Zn2 site. For samples with x = 0.5, 1.0, and 1.5, as the Ni-ion-doping level increases, in comparison to the original crystal structure, the interatomic distances between Zn2 and the corresponding atoms elongate, while the interatomic distances between the corresponding atoms shorten. However, at a doping level of 0.2, the interatomic distances between Zn1 and O atoms increase, and those between Zn2 and O atoms decrease. This behavior is probably a consequence of the fact that at low doping concentrations, Ni²⁺ ions typically disperse uniformly, replacing a small fraction of Zn²⁺ ions in the lattice, thereby imparting localized effects on the crystal structure and properties, with relatively weak interactions among them. At higher Ni²⁺ concentrations, interactions between multiple dopant ions become significant and may begin to influence one another, resulting in the creation of more crystal defects. 48,53,54

In order to test the acid—base resistance of pigments, $Zn_{1.85}Ni_{0.15}SiO_4$ was soaked in acetic acid and ammonia solutions for 6 h. The apparent color of the sample is not changed. There is no obvious peak position and profile change after the acid—base testing, as shown in the XRD patterns of $Zn_{1.85}Ni_{0.15}SiO_4$ (Figure 8). Table 3 lists the L^* a^* b^* values of pigments before and after acid—base testing and calculates the ΔE^* of the samples. When $\Delta E^* \leq 5$, it is considered that there is little change in the pigments. In summary, this indicates that the pigment has promising acid/base resistance.

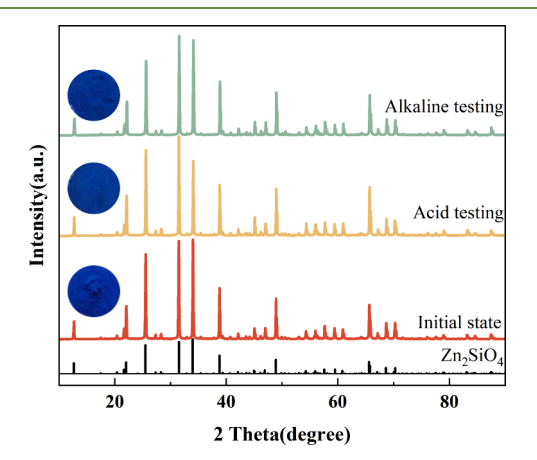


Figure 8. XRD pattern of $\rm Zn_{1.85}Ni_{0.15}SiO_4$ before and after the acid/base resistance test.

Table 3. L^* a^* b^* of $Zn_{1.85}Ni_{0.15}SiO_4$ before and after the Acid/Base Resistance Test

sample	L^*	a*	b*	ΔE^*	
initial state	56.74	8.13	-46.31		
acid testing	56.18	9.84	-43.31	3.50	
alkaline testing	55.78	8.64	-45.41	1.41	
$^{a}\Delta E^{*} = [(\Delta L^{*})^{2} + (\Delta a^{*})^{2} + (\Delta b^{*})^{2}]^{1/2}.$					

3.2. Oxidation State Analysis. To investigate the oxidation state of Ni, the binding energies of elements in Zn_{1.8}Ni_{0.2}SiO₄ were analyzed by XPS analysis. The full survey and enlarged Ni peak are shown in Figure 9. As can be seen from the figure, the characteristic peaks of Zn, Ni, Si, C, and O are displayed in the spectrum. The emergence of the C atomic peak is a consequence of the adsorption of carbon components onto the sample's surface following exposure to air during sample preparation at the time of the test. The main peak of Ni 2p 3/2 is observed at 856.2 eV, and the companion peak possesses a binding energy of 861.6 eV. These values are similar to tetrahedrally coordinated Ni²⁺ in Ni(OH)₂, 55,56 in which the main peak is located at 856.2 eV and the companion peak is at 861.2 eV. Furthermore, researchers conducted an investigation on Ni-doped ZnO with a hexagonal wurtzite structure, where Zn occupies tetrahedral positions. The XPS results indicated that the main peak and satellite peak of Ni 2p 3/2 are situated at ~856.2 and ~861.6 eV, respectively. 57, Thus, the results indicate that the oxidation state of Ni in $Zn_{1.8}Ni_{0.2}SiO_4$ is a +2 oxidation state.

To further prove the oxidation state of Ni ions in the compounds, magnetic susceptibility measurements were conducted on $\mathrm{Zn_{2-x}Ni_xSiO_4}$ (0.05 $\leq x \leq$ 0.2). The results are presented in Figure 10 and Table 4. The inverse magnetic susceptibility exhibits linear variation, fitting the Curie–Weiss law $\chi = C/(T-\theta)$ effectively within the temperature range of 150–300 K.

The experimental effective magnetic moments ($\mu_{\rm eff}$) calculated for Ni-doping levels of 0.1 and 0.2 from the measurement are 3.75 $\mu_{\rm B}$ and 3.64 $\mu_{\rm B}$, respectively. The theoretical magnetic moment of the sample is calculated under two considerations: spin-only case ($\mu_{\rm so}$) and S+L momentum case ($\mu_{\rm S+L}$). When calculated in the spin-only case, the magnetic moment for the Ni atom is 0.61 $\mu_{\rm B}$, while the value for Ni³⁺ is 1.73 $\mu_{\rm B}$. Both of these values are much smaller than that of Ni²⁺ (2.83 $\mu_{\rm B}$). Moreover, the experimental magnetic moment is even higher, indicating that we also need to take S+L momentum into consideration. The experimental values are close to the previous reported values of Ni²⁺ (3.7–4.0 $\mu_{\rm B}$) (Table 5). Thus, the observed magnetic moments for the compounds discussed in Table 4 confirm the presence of Ni in tetrahedral coordination with a + 2 oxidation state (Table 5).

The Weiss constants are -14.92 and -19.55 K, respectively, indicating the presence of antiferromagnetic interactions. ^{59,60} Thus, the magnetic data and the XPS data derive the same conclusion that Ni states in the +2 oxidation state in the compound.

3.3. Optical Performance Analysis. Photographs and color coordinates of $Zn_{2-x}Ni_xSiO_4$ (0.05 $\leq x \leq$ 0.2) and commercial-applied $CoAl_2O_4$ are compared in Figure 11a and Table 6. The chromaticity diagram of $Zn_{2-x}Ni_xSiO_4$ (0.05 $\leq x \leq$ 0.2) is shown in Figure 11b. The colors of as-prepared $Zn_{2-x}Ni_xSiO_4$ (0.05 $\leq x \leq$ 0.2) are bright blue. The color of the pigment obtained in this study is noticeably more vibrant

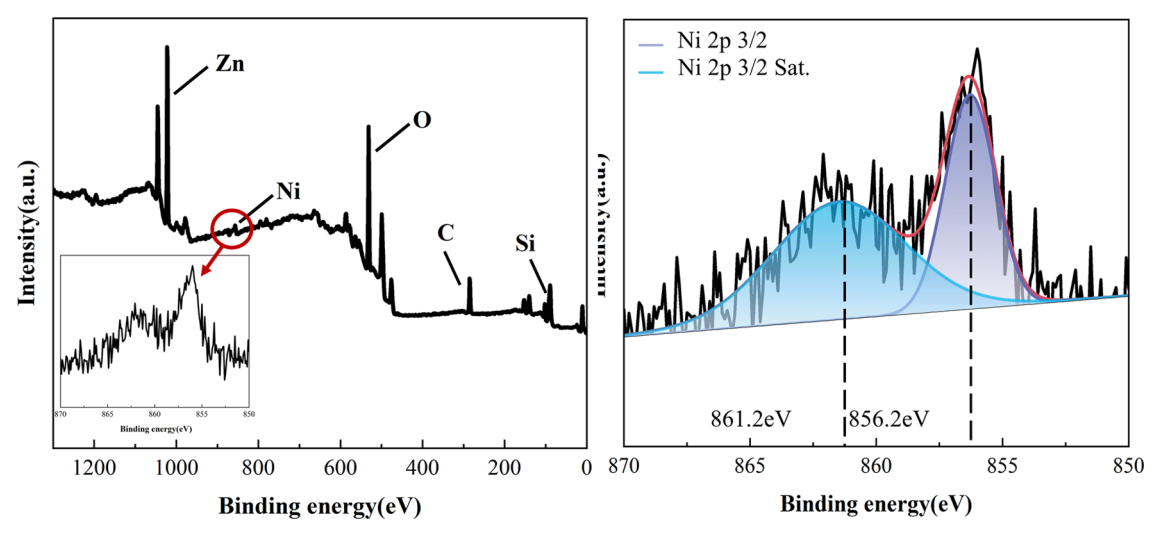


Figure 9. XPS spectra of Zn_{1.8}Ni_{0.2}SiO₄ powders.

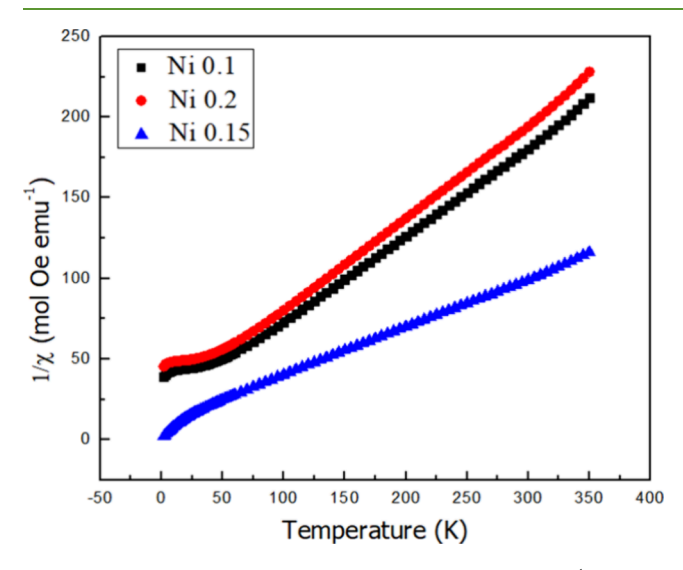


Figure 10. Inverse magnetic susceptibility of $Zn_{2-x}Ni_xSiO_4$ (0.05 $\leq x \leq 0.2$).

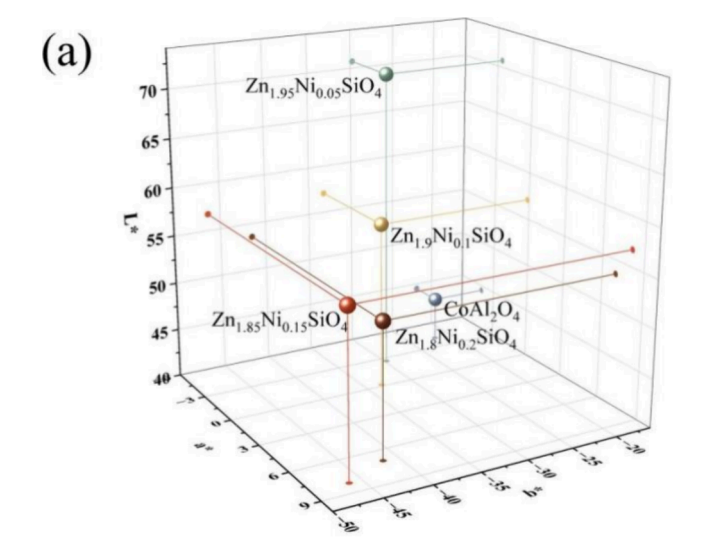
Table 4. Summary of Magnetic Data for the As-Prepared $Zn_{2-x}Ni_xSiO_4$ Sample

composition	th. mag. moment $(\mu_{\rm B})$	Curie constant	Weiss constant (K)	obs. mag. moment $(\mu_{ ext{eff}})$
$Zn_{1.9}Ni_{0.1}SiO_4$	2.83	1.73	-14.92	3.75
$Zn_{1.8}Ni_{0.2}SiO_4$	2.83	1.64	-19.55	3.64

Table 5. Comparison of Calculated Spin-Only (μ_{so}) and Spin Orbital Magnetic Moments (μ_{S+L}) with Experimental Magnetic Data

ion	d configuration	$\mu_{\rm so}/{ m B.M.}$	$\mu_{\rm obs}/{ m B.M.}$	$\mu_{S+L}/B.M.$
Ni(II)	d^8	2.83	3.7-4.0	4.47

than what was previously observed for this structure. 31,42 Furthermore, in comparison to cobalt blue, the as-synthesized pigments demonstrate a higher L^* value and a lower b^* , indicating a stronger blue hue with higher brightness. As the level of Ni doping increases, the a^* value for the pigments rises, indicating the diminishing presence of greenish tones. While the b^* value decreases at the same time, signifying an



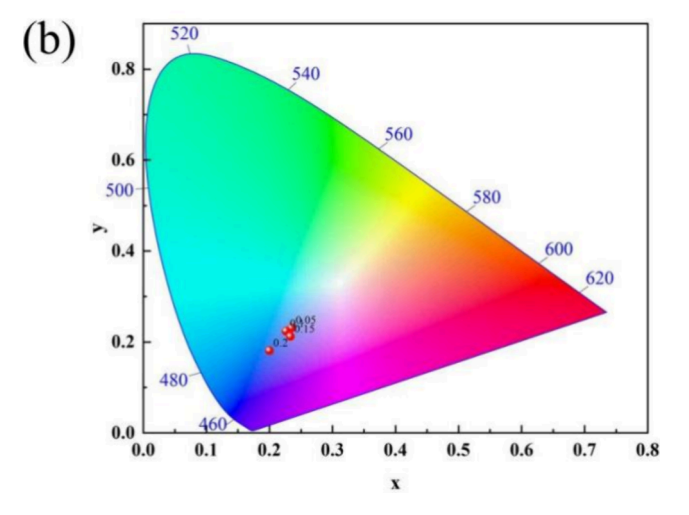


Figure 11. (a) L^* a^* b^* of $\mathrm{Zn_{2-x}Ni_xSiO_4}$ (0.05 $\leq x \leq$ 0.2) and $\mathrm{CoAl_2O_4}$ powders and (b) chromaticity diagram of $\mathrm{Zn_{2-x}Ni_xSiO_4}$ (0.05 $\leq x \leq$ 0.2) powders.

intensified bluish tint. The L^* value gradually diminishes, implying a reduction in the overall brightness. Notably, when the Ni doping level reaches 0.15, the blue chroma reaches its

Table 6. L^* a^* b^* and the Apparent Colors of $Zn_{2-x}Ni_xSiO_4$ (0.05 $\leq x \leq$ 0.2) and $CoAl_2O_4$ Powders

Sample	L^*	a*	<i>b</i> *	Color
Zn _{1.95} Ni _{0.05} SiO ₄	70.70	-2.62	-29.77	
Zn1.9Ni0.1SiO4	57.05	-0.16	-33.25	
$Zn_{1.85}Ni_{0.15}SiO_{4}$	56.74	8.13	-46.31	
Zn _{1.8} Ni _{0.2} SiO ₄	53.59	7.00	-41.54	
CoAl ₂ O ₄	44.46	-4.11	-21.92	

peak, resulting in the most intense and visually striking blue coloration.

The UV-vis-NIR absorption spectra of the $Zn_{2-x}Ni_xSiO_4$ (0.05 $\leq x \leq$ 0.2) solid solution are shown in Figure 12a. For

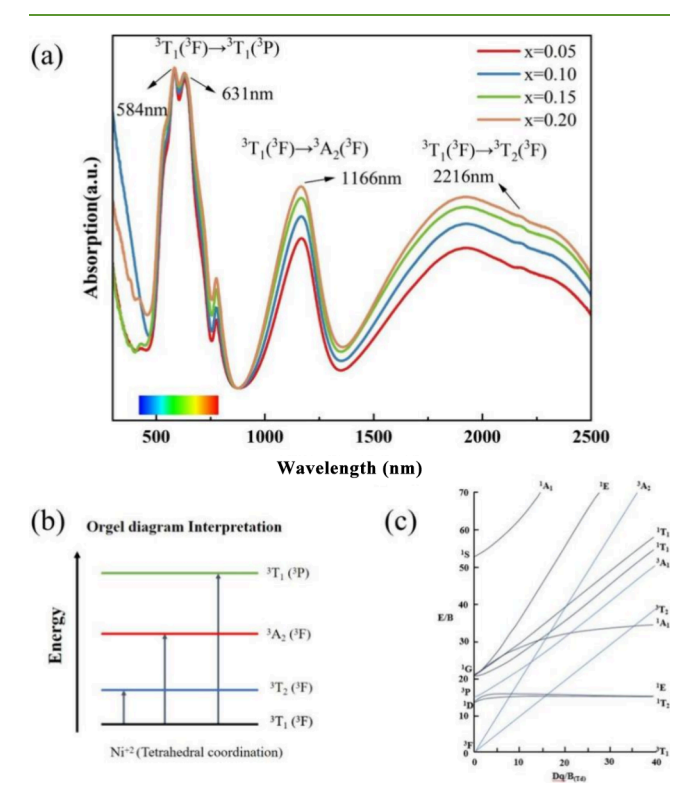


Figure 12. (a) UV-vis-NIR absorbance spectra of $Zn_{2-x}Ni_xSiO_4$ (0.05 $\leq x \leq$ 0.2) powders. (b) Spin-allowed transition for Ni^{2^+} . (c) T-S diagram for Ni^{2^+} (d⁸ electronic configuration) in tetrahedral coordination.

Ni²⁺, with a 3d⁸ configuration, only three transitions are spin-allowed: ${}^3T_1({}^3F) \rightarrow {}^3T_1({}^3P)$, ${}^3T_1({}^3F) \rightarrow {}^3A_2({}^3F)$, ${}^3T_1({}^3F) \rightarrow {}^3T_2({}^3F)$, which correspond to the visible light region, near-infrared region, and far-infrared region, respectively, as shown in Figure 12b. In the visible region, the absorption is due to the d-d transition of Ni²⁺ in tetrahedral coordination. As can be seen from the figure, the sample shows strong absorption at 584 and 631 nm, which are due to the ${}^3T_1({}^3F) \rightarrow {}^3T_1({}^3P)$ transition of Ni^{2+,61-63} This is consistent with the Tanabe–Sugano (T–S) diagram of the d⁸ configuration in the tetrahedral crystal field (Figure 12c). It proves the results from Rietveld refinement that Ni²⁺ replaces Zn²⁺ in the ZnO tetrahedral sites in Zn₂SiO₄ and produces an intense blue

color. The intensity of the absorption peak increases with the increase in Ni^{2+} doping, indicating a decrease in the sample brightness. However, the intensity of the absorption peak is lowest when the Ni^{2+} content is 0.15.

The solar spectrum covers radiance from 200 to 2500 nm (Figure 1), with 52% of the energy located in the near-infrared region. As visible light is responsible for the color, infrared reflectance plays a crucial role in heat insulation (Figure 13).



Figure 13. Schematic diagram of the solar radiation reflective coating roof.

To elucidate the infrared reflectance characteristics of both the blue pigment $Zn_{2-x}Ni_xSiO_4$ and the widely used commercial cobalt blue, a comprehensive comparison is conducted on the NIR Reflectance (R %) and NIR Solar Reflectance (R* %) of $Zn_{2-x}Ni_xSiO_4$ ($0.05 \le x \le 0.2$) and $CoAl_2O_4$, as detailed in Table 7.

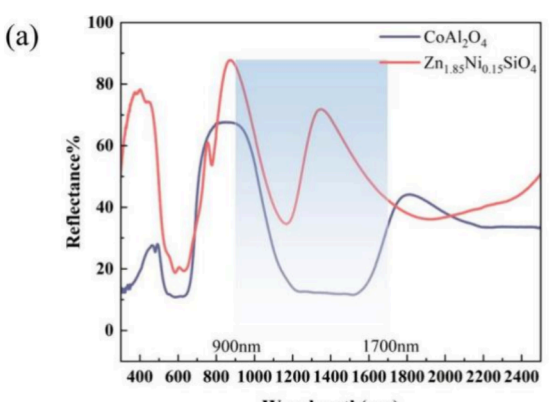
The observed trend reveals a decrease in both NIR Reflectance (R %) and NIR Solar Reflectance (R^* %) of $Zn_{2-x}Ni_xSiO_4$ (0.05 $\leq x \leq$ 0.2) with an increasing amount of Ni doping. However, even with this decrease, the reflectance values remain higher than those of cobalt blue. Particularly in the near-infrared spectral range, the as-synthesized pigments exhibit a notable reflectivity at 876 nm, where the reflectivity reaches its maximum value of 88.77% shown in Figure 14a. The performance attribute underscores why $Zn_{2-x}Ni_xSiO_4$ outperforms cobalt blue. Figure 1 illustrates that the 876 nm peak corresponds to the region with the highest energy in the infrared spectrum, further emphasizing $Zn_{2-x}Ni_xSiO_4$'s superior reflectivity over cobalt blue in this area. Consequently, $Zn_{2-x}Ni_xSiO_4$ demonstrates a higher energy-saving efficiency than cobalt blue.

Figure 14b reveals a notable advantage in the reflection efficiency of $Zn_{2-x}Ni_xSiO_4$ compared to cobalt blue within the wavelength range of 800-1000 nm. $Zn_{2-x}Ni_xSiO_4$ also exhibits high reflection efficiency over cobalt blue in the infrared region of 1200-2500 nm, with reduced energy consumption. Consequently, $Zn_{2-x}Ni_xSiO_4$ emerges as a novel pigment with enhanced reflective properties, surpassing those of cobalt blue.

In addition, a comparative analysis was conducted between the as-synthesized Ni-doped $\rm Zn_2SiO_4$ blue pigment and the other near-infrared pigments, with results presented in Table 8. The comparison reveals that the majority of near-infrared reflective pigments are primarily achieved through $\rm Co^{2+}$ doping. Cobalt, being a scarce resource, experiences rising prices with the expansion of the lithium-ion battery industry. Furthermore, Co-doped pigments do not exhibit significant advantages in terms of infrared reflection efficiency. $^{17,61-63}$ In contrast, the as-synthesized Ni-doped $\rm Zn_2SiO_4$ blue pigments demonstrate superior near-infrared reflective performance, boasting a NIR Solar reflectance of 75.86%. $\rm YIn_{1-x}Mn_xO_3$ demonstrates outstanding infrared reflection properties, with a NIR Solar reflectance reaching as high as 93.33%. However,

Table 7. NIR Reflectance and NIR Solar Reflectance of $Zn_{2-x}Ni_xSiO_4$ (0.05 $\leq x \leq$ 0.2) and $CoAl_2O_4$ Powders

sample	$Zn_{1.95}Ni_{0.05}SiO_4$	$Zn_{1.9}Ni_{0.1}SiO_4$	$Zn_{1.85}Ni_{0.15}SiO_4$	$Zn_{1.8}Ni_{0.2}SiO_4$	$CoAl_2O_4$
R %	63.94	54.82	43.26	39.95	38.54
R* %	75.86	68.84	59.67	54.97	42.95



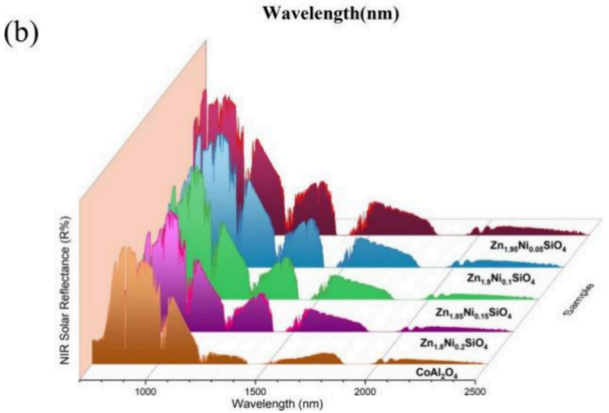


Figure 14. (a) UV–vis–NIR reflectance spectra of $Zn_{1.85}Ni_{0.15}SiO_4$ and $CoAl_2O_4$ powders. (b) NIR solar reflectance spectra of $Zn_{2-x}Ni_xSiO_4$ (0.05 $\leq x \leq$ 0.2) and $CoAl_2O_4$ powders.

the high cost of $\rm In_2O_3$ presents a significant challenge to its commercial viability. On the other hand, $\rm Zn_{2-x}Ni_xSiO_4$, as a silicate pigment, offers the advantages of low cost and possesses certain desirable high infrared reflection properties, thereby presenting promising prospects for large-scale production.

4. CONCLUSIONS

In this work, Ni-doped $Zn_{2-x}Ni_xSiO_4$ (0.05 $\leq x \leq$ 0.2) deep blue pigments were successfully prepared by using a high-temperature solid-state method. The synthesized samples

exhibited pure phases, and a small amount of Ni doping resulted in a noticeable blue coloration. Through XRD refinement and oxidation state analysis, it was confirmed that Ni exists in a divalent form in tetrahedral positions. The discernible blue coloration is attributed to the ${}^{3}T_{1}({}^{3}F) \rightarrow$ ³T₁(³P) transition of Ni²⁺, which is situated at the tetrahedral positions. Compared with previous studies, significantly bluer pigments have been obtained, which may be related to their structure. The pigment exhibited optimal color performance at the Ni-doping level of 0.15 and is stable under acid and alkali conditions. The Zn_{2-x}Ni_xSiO₄ pigments exhibit outstanding reflective properties, particularly in the NIR Solar reflectance, which attains a value of 75.86%, a notable improvement compared to those of currently available blue pigments. The utilization of this innovative blue pigment holds the potential to significantly diminish energy consumption in thermal insulation, consequently fulfilling the objectives of energy conservation and emission reduction. Considering factors such as cost, the Zn_{2-x}Ni_xSiO₄ pigment emerges as a promising cold pigment with significant application potential.

AUTHOR INFORMATION

Corresponding Author

Peng Jiang — School of Materials Science and Engineering, University of Science and Technology Beijing, Beijing 10083, China; orcid.org/0000-0003-3594-5859;

Email: jiangp@ustb.edu.cn

Authors

Qiuying Wang — School of Materials Science and Engineering, University of Science and Technology Beijing, Beijing 10083, China

Zhiwei Wang — School of Materials Science and Engineering, University of Science and Technology Beijing, Beijing 10083, China

Menghang Qi — School of Materials Science and Engineering, University of Science and Technology Beijing, Beijing 10083, China

Hang Zhao — School of Materials Science and Engineering, University of Science and Technology Beijing, Beijing 10083, China

Table 8. NIR Reflectance and NIR Solar Reflectance of Pigments

sample	NIR reflectance (R %)	NIR solar reflectance (R* %)	NIR reflectance (MAX)
CoAl ₂ O ₄ ⁶⁴	51.82		
$Zn_{0.9}Co_{0.1}Al_2O_4^{65}$			58.00 (1100 nm)
2D kaolin/CoAl ₂ O ₄ ⁶⁶	60.18		
$NaZn_{0.9}Co_{0.1}PO_4^{18}$		64.00	
$Sr_{1-x}M_xCuSi_4O_{10} (M = Pr, Nd, Sm)^{67}$			68.54-72.00
$YB_{0.07}Mn_{0.03}O_3^{68}$	69.75		
$YIn_{0.9}Mn_{0.1}O_3-ZnO^{69}$		70	
ultramarine blue (PU) ⁷⁰	80.67		
$YIn_{0.8}Mn_{0.1}(Li/Zn)_{0.1}O_{3-\delta}^{6}$	78.95/72.04	93.33/90.95	92.85/85.12 (1100 nm)
Zn _{2-x} Ni _x SiO ₄ (this study)	38.54-63.94	54.97-75.86	88.77 (876 nm)

- Xin Xin School of Materials Science and Engineering, University of Science and Technology Beijing, Beijing 10083, China
- Anjali Verma Department of Chemistry, Oregon State University, Corvallis, Oregon 97331, United States
- Theeranun Siritanon School of Chemistry, Institute of Science, Suranaree University of Technology, Nakhon Ratchasima 30000, Thailand; orcid.org/0000-0002-5076-2367
- Arthur P. Ramirez Department of Physics, University of California, Santa Cruz, California 95064, United States
 M.A. Subramanian Department of Chemistry, Oregon State
 University, Corvallis, Oregon 97331, United States;
 orcid.org/0000-0001-5487-043X

Complete contact information is available at: https://pubs.acs.org/10.1021/acssuschemeng.3c07982

Notes

The authors declare no competing financial interest.

ACKNOWLEDGMENTS

This work was sponsored by the Beijing Nova Program under the grant number of 20230484282, the Fundamental Research Funds for the Central Universities under the grant number of FRF-IDRY-22-011, and Youth Teacher International Exchange & Growth Program under grant No. 20230004. The work done at the Oregon State University is supported by US National Science Foundation Grant No. DMR-2025615.

REFERENCES

- (1) Huang, B.; Xiao, Y.; Zhou, H.; Chen, J.; Sun, X. Synthesis and Characterization of Yellow Pigments of $Bi_{1.7}RE_{0.3}W_{0.7}Mo_{0.3}O_6(RE=Y,Yb,Gd,Lu)$ with High NIR Reflectance. ACS Sustainable Chem. Eng. **2018**, 6 (8), 10735–10741.
- (2) Fortuño-Morte, M.; Serna-Gallén, P.; Beltrán-Mir, H.; Cordoncillo, E. A new series of environment-friendly reddish inorganic pigments based on AFeO₃ (A = Ln, Y) with high NIR solar reflectance. *Journal of Materiomics* **2021**, 7 (5), 1061–1073.
- (3) Li, L.; Feng, L.; Xiao, Y.; Xie, W.; Sun, X. Synthesis and Characterization of Yellow Pigments (Li_{0.4}RE_{0.6}Al_{0.6})₁₂MoO₄–BiVO₄ with High NIR Reflectance. ACS Sustainable Chem. Eng. **2021**, 9 (49), 16606–16616.
- (4) Feng, L.; Li, L.; Zhang, M.; Yang, Y.; Sun, X. Novel and environment-friendly high NIR reflectance color pigments based on Fe, Pr, Ho, Nd, Er and Ce doped lithium aluminum molybdate: Synthesis and properties. *Ceram. Int.* **2022**, 48 (20), 30630–30639.
- (5) Znang, M.; Yang, Y.; Feng, L.; Sun, X. Synthesis and characterization of Fe³⁺ doped YIn_{1-y}Mn_yO₃ black pigment with high near-infrared reflectance. *Ceram. Int.* **2023**, *49*, 19290–19300.
- (6) Zhang, M.; Feng, L.; Zeng, Z.; Yang, Y.; Sun, X. Environmentally Friendly High-Near-Infrared Reflectance Blue Pigment $YIn_{0.9-x}Mn_{0.1}M_xO_{3-\delta}$ Based on Li/Zn Doping. ACS Sustainable Chem. Eng. 2022, 10 (41), 13877–13886.
- (7) Berardi, U. A cross-country comparison of the building energy consumptions and their trends. *Resources, Conservation and Recycling* **2017**, *123*, 230–241.
- (8) Peng, Y.; Lai, J.-C.; Xiao, X.; Cui, Y.; et al. Colorful low-emissivity paints for space heating and cooling energy savings. *Proc. Natl. Acad. Sci. U. S. A.* **2023**, *120* (34), No. e2300856120.
- (9) Sudhaik, A.; Parwaz Khan, A. A.; Raizada, P.; Nguyen, V. H.; Van Le, Q.; Asiri, A. M.; Singh, P. Strategies based review on near-infrared light-driven bismuth nanocomposites for environmental pollutants degradation. *Chemosphere* **2022**, *291* (Pt 2), No. 132781.

- (10) Jose, S.; Joshy, D.; Narendranatha, S. B.; Periyat, P. Recent advances in infrare dreflective inorganic pigments. *Sol. Energy Mater. Sol. Cells* **2019**, 194, 7–27.
- (11) Pfaff, G. Ultramarine pigments. *Physical Sciences Reviews* **2021**, 6 (12), 879–885.
- (12) Tan, L.; Wang, Q.; Cheng, Z.; Hu, Z.; Liu, K.; Wang, Y.; Chang, Q. Research on the low-temperature synthesis of cobalt aluminum spinel type blue pigments. *J. Alloys Compd.* **2021**, 864 (25), No. 158625.
- (13) Yoneda, M.; Gotoh, K.; Nakanishi, M.; Fujii, T.; Nomura, T. Influence of aluminum source on the color tone of cobalt blue pigment. *Powder Technol.* **2018**, 323, 574–580.
- (14) Smith, A. E.; Mizoguchi, H.; Delaney, K.; Spaldin, N. A.; Sleight, A. W.; Subramanian, M. A. Mn³⁺ in Trigonal Bipyramidal Coordination A New Blue Chromophore. *J. Am. Chem. Soc.* **2009**, *131* (47), 17084–17086.
- (15) Liu, L.; Li, M.; Jiang, P.; Cui, K.; Wang, Y.; Kuang, J.; Cao, W. Study on the synthesis and optical properties of YIn_{1-x}Mn_xO₃ by N/S doping. *Solid State Sci.* **2021**, *113*, No. 106516.
- (16) Aguilar-Elguézabal, A.; Román-Aguirre, M.; De la Torre-Sáenz, L.; Pizá-Ruiz, P.; Bocanegra-Bernal, M. Synthesis of CoAl₂O₄/Al₂O₃ nanoparticles for ceramic blue pigments. *Ceram. Int.* **2017**, 43 (17), 15254–15257.
- (17) Primo, J. d. O.; Horsth, D. F. L.; Balaba, N.; Umek, P.; Anaissi, F. J.; Bittencourt, C. Synthesis of Blue Gahnite (ZnAl₂O₄:Co, Nd): A Cost-Effective Method for Producing Solar-Reflective Pigments for Cool Coatings. *Materials* **2023**, *16* (4), 1696.
- (18) Thejus, P. K.; Krishnapriya, K. V.; Nishanth, K. G. A cost-effective intense blue colour inorganic pigment for multifunctional cool roof and anticorrosive coatings. *Sol. Energy Mater. Sol. Cells* **2021**, 219, No. 110778.
- (19) Costa, G.; Ribeiro, M. J.; Hajjaji, W.; Seabra, M. P.; Labrincha, J. A.; Dondi, M.; Cruciani, G. Ni-doped hibonite (CaAl₁₂O₁₉): A new turquoise blue ceramic pigment. *Journal of the European Ceramic Society* **2009**, 29 (13), 2671–2678.
- (20) Bhim, A.; Laha, S.; Gopalakrishnan, J.; Natarajan, S. Color Tuning in Garnet Oxides: The Role of Tetrahedral Coordination Geometry for 3 d Metal Ions and Ligand-Metal Charge Transfer (Band-Gap Manipulation). *Chemistry An Asian Journal* **2017**, *12* (20), 2734–2743.
- (21) Wang, Y.; Lei, H.; Jiang, P.; Liu, L.; Cui, K.; Cao, W. Synthesis and optical properties of intense blue colors oxides based on Mn⁵⁺ in tetrahedral sites in Ba₇Al₂-Mn O¹⁰⁺. *Ceram. Int.* **2021**, 47 (1), 686–691.
- (22) Medina, E. A.; Li, J.; Stalick, J. K.; Subramanian, M. A. Intense turquoise colors of apatite-type compounds with Mn⁵⁺ in tetrahedral coordination. *Solid State Sci.* **2016**, *52*, 97–105.
- (23) Li, J.; Medina, E. A.; Stalick, J. K.; Sleight, A. W.; Subramanian, M. A. Colored oxides with hibonite structure A potential route to non-cobalt blue pigments. *Prog. Solid State Chem.* **2016**, *44* (4), 107–122.
- (24) Wang, Y.; Cheng, Q.; Jiang, P.; Liu, L.; Cui, K.; Li, Y. Synthesis and properties of novel blue zirconia ceramic based on Co/Ni-doped BaAl₁₂O₁₉ blue chromophore. *Journal of the European Ceramic Society* **2022**, 42 (2), 543–551.
- (25) Ianoş, R.; Barvinschi, P. Characterization of $Mg_{1-x}Ni_xAl_2O_4$ solid solutions prepared by combustion synthesis. *Journal of the European Ceramic Society* **2011**, 31 (5), 739–743.
- (26) Tamilarasan, S.; Reddy, M. L.; Natarajan, S.; Gopalakrishnan, J. Developing Intense Blue and Magenta Colors in alpha-LiZnBO₃: The Role of 3d-Metal Substitution and Coordination. *Chem. Asian J.* **2016**, 11 (22), 3234–3240.
- (27) Thieme, C.; Waurischk, T.; Lin, C.; Rüssel, C. Lilac ceramic pigments based on $Ba_{0.5}Sr_{0.5}Zn_{2-x}Ni_xSi_2O_7$ solid solutions. *Ceram. Int.* **2016**. 42 (11), 13035–13040.
- (28) Goetz, G.; Roussos, G.; Schulz, H.-J. Spin-orbit interaction in the ground state multiplet of the Ni²⁺(d⁸) Ion in II-VI semi-conductors. *Solid State Commun.* **1986**, *57* (5), 343–346.

- (29) Weakliem, H. A. Optical Spectra of Ni²⁺, Co²⁺, and Cu²⁺ in Tetrahedral Sites in Crystals. *J. Chem. Phys.* **1962**, 36 (8), 2117–2140.
- (30) Ibreva, T.; Dimitrov, T.; Markovska, I. Synthesis and study of Ni-doped willemite ceramic pigments. In *57th Annual scientific conference of University of Ruse and Union of Scientists*; 2018; pp 173–178.
- (31) Dimitrov, T. I.; Markovska, I. G.; Ibreva, T. H. The Analysis about Synthesis, Structure and Properties of Willemite Ceramic Pigments Obtained by a Sol—Gel Method. *IOP Conference Series: Materials Science and Engineering* **2020**, 893 (1), No. 012001.
- (32) Zhang, S.; Lu, M.; Li, Y.; Sun, F.; Yang, J.; Wang, S. Synthesis and electrochemical properties of Zn₂SiO₄ nano/mesorods. *Mater. Lett.* **2013**, *100*, 89–92.
- (33) Lukić, S. R.; Petrović, D. M.; Đačanin, L. J.; et al. Gelcombustion synthesis of transition metalions doped Zn₂SiO₄ powder. *J. Optoelectron. Adv. Mater.* **2008**, *10* (10), 2748–2752.
- (34) Chandra Babu, B.; Buddhudu, S. Analysis of structural and electrical properties of Ni²⁺:Zn₂SiO₄ ceramic powders by sol–gel method. *J. Sol-Gel Sci. Technol.* **2014**, 70 (3), 405–415.
- (35) Masjedi-Arani, M.; Salavati-Niasari, M. A simple sonochemical approach for synthesis and characterization of Zn₂SiO₄ nanostructures. *Ultrason Sonochem* **2016**, *29*, 226–235.
- (36) Chandra Babu, B.; Wang, G.-G.; Yan, B.; Yang, Q.; Baker, A. P. Effects of Cr^{3+} addition on the structure and optical properties of α -Zn₂SiO₄ synthesized by sol-gel method. *Ceram. Int.* **2018**, *44*, 938–946
- (37) Dai, R.; Cheng, R.; Wang, J.; Zhang, C.; Li, C.; Wang, H.; Wang, X.; Zhou, Y. Tunnel-structured willemite Zn₂SiO₄ Electronic structure, elastic, and thermal properties. *J. Adv. Ceram.* **2022**, *11* (8), 1249–1262.
- (38) Singh, V.; Prasad, A.; Deopa, N.; et al. Luminescence features of Mn²⁺-doped Zn₂SiO₄ A green color emitting phosphor for solid-state lighting. *Optik* **2021**, 225, No. 165715, DOI: 10.1016/j.ijleo.2020.165715.
- (39) Takesue, M.; Hayashi, H.; Smith, R. L. Thermal and chemical methods for producing zinc silicate (willemite): A review. *Progress in Crystal Growth and Characterization of Materials* **2009**, 55 (3–4), 98–124.
- (40) Diao, C.-C.; Yang, C.-F. Synthesis of high efficiency Zn₂SiO₄:Mn²⁺ green phosphors using nano-particles. *Ceram. Int.* **2010**, 36 (5), 1653–1657.
- (41) Portakal-Uçar, Z. G.; Dogan, T.; Akça, S.; Kaynar, Ü. H.; Topaksu, M. Effect of Sm³⁺ and Mn²⁺ incorporation on the structure and luminescence characteristics of Zn₂SiO₄ phosphor. *Radiat. Phys. Chem.* **2021**, *181*, No. 109329, DOI: 10.1016/j.radphyschem.2020.109329.
- (42) Babu, B. C.; Kumar, K. N.; Rudramadevi, B. H.; Buddhudu, S. Synthesis, Structural and Dielectric Properties of Co²⁺, Ni²⁺and Cu²⁺:Zn₂SiO₄ Nanoceramics by a Sol-gel Method. *Ferroelectrics Letters Section* **2014**, *41* (1–3), 28–43.
- (43) Lavat, A. E.; Gayo, G. X. In situ formation of coloured M(II)–doped Zn_2SiO_4 –willemite in ceramic glazes (M = Mn, Co, Ni, Cu). *Ceram. Int.* **2014**, *40* (8), 11947–11955.
- (44) Lee, C.-Y.; Lee, H.-S.; Lee, B.-H. A Study on the NiO-doped Willemite Pigments. *Journal of the Korean Ceramic Society* **2011**, 48 (2), 134–140.
- (45) Lukić, S. R.; Petrović, D. M.; Đačanin, L. Gelcombustion synthesis of transition metalions doped Zn₂SiO₄ powder-JOAM. *J. Optoelectron. Adv. Mater.* **2008**, *10* (10), 2748–2752.
- (46) Rodríguez-Carvajal, J. Recent advances in magnetic structure determination by neutron powder diffraction. *Physica B: Condensed Matter* **1993**, 192 (1–2), 55–69.
- (47) Mohapatra, J.; Mishra, D. K.; Kamilla, S. K.; et al. Ni-doped ZnO Studies on structural and magnetic properties. *Phys. Status Solidi* **2011**, 248 (6), 1352–1359.
- (48) Rana, A. K.; Kumar, Y.; Rajput, P.; Jha, S. N.; Bhattacharyya, D.; Shirage, P. M. Search for Origin of Room Temperature Ferromagnetism Properties in Ni-Doped ZnO Nanostructure. *ACS Appl. Mater. Interfaces* **2017**, *9* (8), 7691–7700.

- (49) Ahmed, M. A.; Rady, K. E.; Shams, M. S. Enhancement of electric and magnetic properties of Mn–Zn ferrite by Ni–Ti ions substitution. *J. Alloys Compd.* **2015**, 622, 269–275.
- (50) Shannon, R. D. Revised Effective Ionic Radii and Systematic Studies of Interatomie Distances in Halides and Chaleogenides. *Acta Crystallogr. Sect. A: Cryst. Phys.*, Diffr., Theor. Gen. Crystallogr. 1976, 32 (5), 751–767.
- (51) Benchikhi, M.; Hattaf, R.; Moutaabbid, A.; El Ouatib, R. Structural, morphological, and optical properties of Co- substituted Zn₂SiO₄ nanopowders prepared by a hydrothermal-assisted sol-gel process. *Mater. Chem. Phys.* **2022**, 276, No. 125434, DOI: 10.1016/j.matchemphys.2021.125434.
- (52) Srinivas, K.; Manjunath Rao, S.; Venugopal Reddy, P. Preparation and properties of Zn_{0.9}Ni_{0.1}O diluted magnetic semi-conductor nanoparticles. *J. Nanopart. Res.* **2011**, *13* (2), 817–837.
- (53) G K, P.; Prashanth, P. A.; Singh, P.; Nagabhushana, B. M.; Shivakumara, C.; G M, K.; Nagendra, H. G.; Sathyananda, H. M.; Chaturvedi, V. Effect of doping (with cobalt or nickel) and UV exposure on the antibacterial, anticancer, and ROS generation activities of zinc oxide nanoparticles. *Journal of Asian Ceramic Societies* 2020, 8 (4), 1175–1187.
- (54) Anandan, S.; Muthukumaran, S. Microstructural, crystallographic and optical characterizations of Cu-doped ZnO nanoparticles co-doped with Ni. *Journal of Materials Science: Materials in Electronics* **2015**, 26 (6), 4298–4307.
- (55) Nesbitt, H. W.; Bancroft, G. M; Legrand, D. Interpretation of Ni2p XPS spectra of Ni conductors and Ni insulators. *Phys. Chem. Miner.* **2000**, *27*, 357–366.
- (56) Singh Yadav, R.; Havlica, J.; Masilko, J.; Kalina, L.; Wasserbauer, J.; Hajdúchová, M.; Enev, V.; Kuřitka, I.; Kožáková, Z. Effects of annealing temperature variation on the evolution of structural and magnetic properties of NiFe₂O₄ nanoparticles synthesized by starch-assisted sol—gel auto-combustion method. *J. Magn. Magn. Mater.* **2015**, 394, 439–447.
- (57) Zhong, M.; Li, Y.; Tariq, M.; Hu, Y.; Li, W.; Zhu, M.; Jin, H.; Li, Y. Effect of oxygen vacancy induced by pulsed magnetic field on the room-temperature ferromagnetic Ni-doped ZnO synthesized by hydrothermal method. *J. Alloys Compd.* **2016**, *675*, 286–291.
- (58) Zhang, N.; Li, H.; Xu, Z.; Yuan, R.; Xu, Y.; Cui, Y. Enhanced Acetone Sensing Property of a Sacrificial Template Based on Cubic-Like MOF-5 Doped by Ni Nanoparticles. *Nanomaterials* **2020**, *10* (2), 386 DOI: 10.3390/nano10020386.
- (59) Knyrim, J. S.; Friedrichs, J.; Neumair, S.; Roeßner, F.; Floredo, Y.; Jakob, S.; Johrendt, D.; Glaum, R.; Huppertz, H. High-pressure syntheses and characterization of the transition metal borates β -MB₄O₇ (M = Mn²⁺, Ni²⁺, Cu²⁺). *Solid State Sci.* **2008**, *10* (2), 168–176.
- (60) Qin, B.; Zhang, X.; Zhang, J. A New Multifunctional Zinc–Organic Framework with Rare Interpenetrated Tripillared Bilayers as a Luminescent Probe for Detecting Ni²⁺ and PO₄³⁻ in Water. *Cryst. Growth Des.* **2020**, 20 (8), 5120–5128.
- (61) Singh, S.; Rama, N.; Ramachandra Rao, M. S. Influence of d-d transition bands on electrical resistivity in Ni doped polycrystalline ZnO. *Appl. Phys. Lett.* **2006**, 88 (22), 222111 DOI: 10.1063/1.2208563.
- (62) Chandrappa, G. T.; Ghosh, S.; Patil, K. C. Synthesis and Properties of Willemite, Zn_2SiO_4 , and M^{2+} : Zn_2SiO_4 (M = Co and Ni). *Journal of Materials Synthesis and Processing* **1999**, 7 (5), 273–279.
- (63) Ullrich, K.; Locmelis, S.; Binnewies, M.; Becker, K. D. An Optical Spectroscopy Study of Ionic Defects: Ni²⁺ Ions in Tetrahedral Coordination. *Phase Transitions* **2003**, *76* (1–2), 103–116.
- (64) Ali, A. A.; El Fadaly, E.; Ahmed, I. S. Near-infrared reflecting blue inorganic nano-pigment based on cobalt aluminate spinel via combustion synthesis method. *Dyes Pigm.* **2018**, *158*, 451–462.
- (65) Ianoş, R.; Muntean, E.; Păcurariu, C.; Lazău, R.; Bandas, C.; Delinescu, G. Combustion synthesis of a blue Co-doped zinc aluminate near-infrared reflective pigment. *Dyes Pigm.* **2017**, *142*, 24–31.

- (66) Liu, W.; Du, T.; Ru, Q.; Zuo, S.; Yang, X.; Yao, C.; Kong, Y. Facile synthesis and characterization of 2D kaolin/CoA₂O₄: A novel inorganic pigment with high near-infrared reflectance for thermal insulation. *Appl. Clay Sci.* **2018**, *153*, 239–245.
- (67) Jing, J.; Zhang, Y.; Sun, J.; Zhao, X.; Gao, D.; Zhang, Y. A comparative study on different RE-doped (RE = Pr, Nd, Sm) $SrCuSi_4O_{10}$ blue pigments with high near-infrared reflectance. *Dyes Pigm.* **2018**, *150*, 9–15.
- (68) Fang, P.; Zhou, S.; Liu, Y.; Ye, J.; Wang, L.; Li, C.; Zhuo, S.; Chen, W. Solution combustion synthesis of gray-blue Mn-doped YBO₃ pigments with high NIR reflectance for energy-saving buildings. *Ceram. Int.* **2022**, *48* (24), 37203–37211.
- (69) Jose, S.; Jayaprakash, A.; Laha, S.; Natarajan, S.; Nishanth, K. G.; Reddy, M. L. P. YIn_{0.9}Mn_{0.1}O₃–ZnO nano-pigment exhibiting intense blue color with impressive solar reflectance. *Dyes Pigm.* **2016**, 124, 120–129.
- (70) Lv, C.; Zu, M.; Xie, D.; Liu, D.; Cheng, H. Ellipsoid ultramarine blue pigment with high near-infrared reflectance. *Mater. Today Commun.* **2021**, 27, No. 102267, DOI: 10.1016/j.mtcomm.2021.102267.